Magnetic-Thermal Coupling Analysis of Saturable Reactor

Yifan Chen[1,2], Qingxin Yang[1,2], Changgeng Zhang[1,2], Yongjian Li[1,2], and Jiajun Wang[1,2]

[1]State Key Laboratory of EERI, School of Electrical Engineering, Hebei University of Technology, Tianjin 300130, China
[2]Hebei Province School of Key Laboratory of EFEAR, Hebei University of Technology, Tianjin 300130, China

As the vital equipment of ultra-high voltage direct current (UHVDC) transmission, the anodic saturable reactor is crucial to the safe operation of converter valve. Based on dynamic core loss model, the eddy current analysis and core loss calculation on saturable reactor are carried out by finite-element method (FEM) simulation software Maxwell. Through the fast-mapping interpolation method between heterogeneous meshes, the core loss is mapped from electromagnetic field to the fluid field by Fluent user-defined functions (UDFs), which makes the distribution of heat source more realistic. The distributions of temperature and velocity of the anodic saturable reactor are obtained by computational fluid dynamics (CFD) simulation software Fluent. The temperature simulation results show that the hottest spots inside the core and on the reactor inner toroidal surface are 117.4 °C and 80.5 °C, respectively. The experimental results demonstrate the validity of the calculation methods of core loss and temperature distribution.

***Index Terms*— Anodic saturable reactor, dynamic core loss model, heterogeneous meshes mapping, temperature distribution.**

I. Introduction

THE anodic saturable reactor is a critical element in the thyristor converter valve of high voltage direct current (HVdc) transmission system, which is designed to limit rapid current rise of the thyristor and protect it from being damaged [1], [2]. However, the non-uniform distribution of core loss of anodic saturable reactor can cause local overheating and thermal aging of insulating material, and eventually lead to failure. Because it is difficult to measure the local core loss of anodic saturable reactor directly, the infrared thermal imager is used for real-time temperature monitoring [3]. The classical Steinmetz equation and Bertotti loss separation model are only suitable to sinusoidal excitation and cannot be applied in this complex impulse excitation current of saturable reactor [4], [5]. Therefore, the dynamic core loss calculation method is adopted to calculate core loss of the reactor [6]–[9].

In this article, the loss parameters are extracted by curves fitting and the model of saturable reactor is established for core loss analysis by electromagnetic finite-element method (FEM). To share the data between the magnetic field and temperature field accurately, the core loss is mapped between heterogeneous meshes [10]–[12]. Based on the calculation results of computational fluid dynamics (CFD), the steady-state temperature distribution is obtained. The effectiveness of the simulation model is verified by the temperature experiment.

II. Anodic Saturable Reactor Model

As shown in Fig. 1(a), the main components of the reactor are core and windings. Five turns of hollow aluminum tubes are cast with epoxy resin and nine pairs of U-shaped cores are put on it. Then put them in a fiberglass shell filled with polyurethane elastomer. The windings made of aluminum tubes are cooled by circulated water inside. To save computing resource, one in nine model shown in Fig. 1(b) is adopted for electromagnetic and temperature analysis.

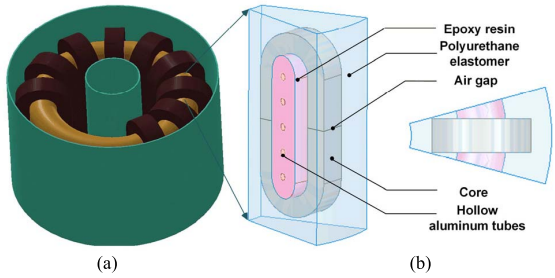


Fig. 1. Establishment of anodic saturable reactor model. (a) Actual model of saturable reactor. (b) One in nine model.

III. Electromagnetic Loss Calculation

Core loss of anodic saturable reactor includes hysteresis loss, eddy current loss and excess loss. The core loss distribution is influenced by the excitation current, air gap and the structure of reactor. For this model, Maxwell's equations in the eddy current field are as follows:

$$\nabla \times \left(\frac{1}{\mu}\nabla \times \boldsymbol{A}\right) = -\sigma\left(\frac{\partial \boldsymbol{A}}{\partial t} + \nabla\varphi\right) \tag{1}$$

$$\nabla \cdot \left(\sigma\frac{\partial \boldsymbol{A}}{\partial t} + \sigma\nabla\varphi\right) = 0 \tag{2}$$

where $\boldsymbol{A}$ is the magnetic vector potential, φ is the electric scalar potential, μ is the magnetic permeability tensor, and σ is the electric conductivity.

A. Impulse Excitation Current

Considering whether or not the reactor being saturable, the impulse excitation current during one cycle can be divided into three stages in Fig. 2. In the first stage, the current

Manuscript received March 23, 2021; revised May 6, 2021; accepted May 11, 2021. Date of publication May 25, 2021; date of current version January 20, 2022. Corresponding author: C. Zhang (e-mail: changgeng.zhang@hebut.edu.cn).

Color versions of one or more figures in this article are available at https://doi.org/10.1109/TMAG.2021.3083649.

Digital Object Identifier 10.1109/TMAG.2021.3083649

0018-9464 © 2021 IEEE. Personal use is permitted, but republication/redistribution requires IEEE permission.
See https://www.ieee.org/publications/rights/index.html for more information.

Authorized licensed use limited to: Hebei University of Technology. Downloaded on February 20,2022 at 13:09:28 UTC from IEEE Xplore. Restrictions apply.

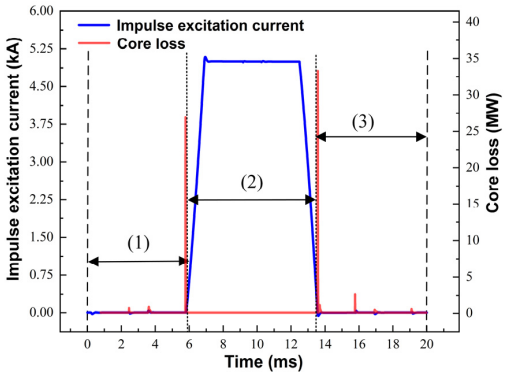


Fig. 2. Impulse excitation current during one cycle.

increases sharply at $t = 5.8$ ms, resulting in high magnetic flux density changing rate (dB/dt). With the transformation from unsaturated state to saturated state, core loss increases gradually. In the second stage, the core has reached saturated state and dB/dt inside core is near zero, although the current even rises to 5 kA at $t = 6.9$ ms, and then drops at $t = 12.4$ ms. Therefore, no core loss is generated during this stage. In the third stage, the core turns into unsaturated state at $t = 13.5$ ms and core loss is generated by rapidly decreasing current again.

B. Loss Coefficients of Ultra-Thin Silicon Steel

The general methods for core loss calculation are Steinmetz equation and Bertotti loss separation model. It is considered that core loss is only related to electrical conductivity σ, sinusoidal excitation frequency f, and peak magnetic flux density B_{m}. The volume density of core loss P_{v} by these two models can be expressed in (3) and (4). k_{m}, α, and β in (3) are the empirical coefficients of Steinmetz equation. k_{h}, k_{c}, and k_{e} in (4) denote the hysteresis loss coefficient, eddy current loss coefficient and excess loss coefficient, respectively,

$$P_{\mathrm{v}} = k_{\mathrm{m}} f^{\alpha} B_{\mathrm{m}}^{\beta} \tag{3}$$

$$P_{\mathrm{v}} = k_{\mathrm{h}} f B_{\mathrm{m}}^{\beta} + k_{\mathrm{c}} (f B_{\mathrm{m}})^2 + k_{\mathrm{e}} (f B_{\mathrm{m}})^{1.5}. \tag{4}$$

The value of parameter β in (4) is always assigned as 2 [6]. So (4) can be written as

$$\begin{aligned} P_{\mathrm{v}} &= (k_{\mathrm{h}} f + k_{\mathrm{c}} f^2) B_{\mathrm{m}}^2 + (k_{\mathrm{e}} f^{1.5}) B_{\mathrm{m}}^{1.5} \\ &= K_1 B_{\mathrm{m}}^2 + K_2 B_{\mathrm{m}}^{1.5}. \end{aligned} \tag{5}$$

The B–P curves of ultra-thin silicon steel under 50–1000 Hz are measured by Epstein frame. The least square method is used for fitting analysis. Equation (6) is taken as the fitting function error. P_{si} and B_{mi} are the data corresponding to point i of the B–P curves

$$\mathrm{err}(K_1, K_2) = \sum_i \left[P_{si} - \left(K_1 B_{mi}^2 + K_2 B_{mi}^{1.5} \right) \right]^2. \tag{6}$$

Eddy current loss coefficient k_{c} can be calculated by the following equation, where d is thickness and ρ represents mass density:

$$k_{\mathrm{c}} = \pi^2 \sigma \frac{d^2}{6\rho}. \tag{7}$$

TABLE I
CORE LOSS COEFFICIENTS OF ULTRA-THIN SILICON STEEL

k_h [W/m^3]	k_c [W/m^3]	k_e [W/m^3]
80.6902	0.0365	1.7582

By substituting K_1, K_2, k_{c}, and f_0 into (8) and (9), k_{h} and k_{e} can be obtained and their values are shown in Table I

$$k_{\mathrm{h}} = \frac{K_1 - k_{\mathrm{c}} f_0^2}{f_0} \tag{8}$$

$$k_{\mathrm{e}} = \frac{K_2}{f_0^{1.5}}. \tag{9}$$

C. Dynamic Core Loss Calculation Method

If the core loss coefficients under various frequencies are adopted directly, the discontinuous breakpoints may appear at the boundary joints of each frequency range [8]. To solve this, the method of equivalent elliptical loop (EEL) is adopted to model the hysteresis loop in time domain, which can consider the loss caused by small loop [9]. Therefore, the calculation accuracy of dynamic hysteresis loss is improved. In this method, the hysteresis loss p_{h}, eddy loss p_{c}, and excess loss p_{e} can be expressed as follows:

$$p_{\mathrm{h}}(t) = \frac{1}{\pi} k_{\mathrm{h}} B_{\mathrm{m}} \cos(\theta) \frac{dB}{dt} \tag{10}$$

$$p_{\mathrm{c}}(t) = \frac{1}{2\pi^2} k_{\mathrm{c}} \left(\frac{dB}{dt} \right)^2 \tag{11}$$

$$p_{\mathrm{e}}(t) = \frac{1}{C_{\mathrm{e}}} k_{\mathrm{e}} \left| \frac{dB}{dt} \right|^{1.5} \tag{12}$$

where the constant C_{e} can be calculated by the following equation, and θ represents the polar angle of the ellipse loop:

$$C_{\mathrm{e}} = (2\pi)^{1.5} \frac{2}{\pi} \int_0^{\frac{\pi}{2}} \cos^{1.5}(\theta) d\theta = 8.763363. \tag{13}$$

D. Dynamic Core Loss Calculation Method

To reduce eddy current loss, the core is made of ultra-thin silicon steel sheets with 0.1 mm thickness. As shown in Fig. 3, the leakage magnetic flux penetrates the silicon steel normally, so the outermost layers silicon steel sheets have significant eddy current. However, the exact laminated core model consisted of sheet-by-sheet ultra-thin silicon steel is difficult to compute.

To simplify the calculation, the homogenization model is adopted. Additionally, the core can be partitioned into blocks with different meshing criteria based on the skin depth δ in (14). The finer mesh is applied to the regions near the core surfaces and the air gaps where the gradient of magnetic flux density is larger. By contrast, the rougher mesh is carried out inside the core where electromagnetic field cannot penetrate. The influence of material anisotropy is also considered

$$\delta = \sqrt{\frac{1}{\pi f \mu \sigma}}. \tag{14}$$

Authorized licensed use limited to: Hebei University of Technology. Downloaded on February 20,2022 at 13:09:28 UTC from IEEE Xplore. Restrictions apply.

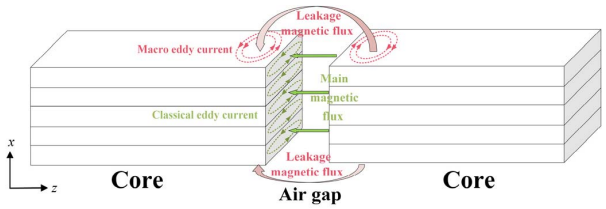


Fig. 3. Eddy current loss at airgap between two U-shape cores.

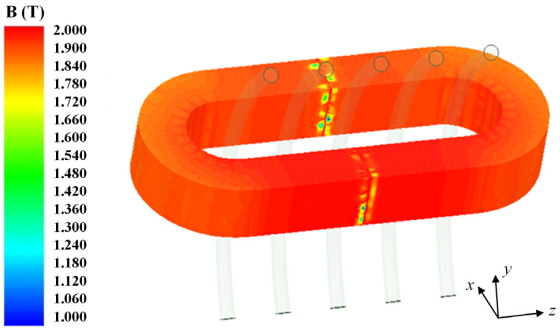


Fig. 4. Distribution of magnetic flux density at $t = 6.9$ ms.

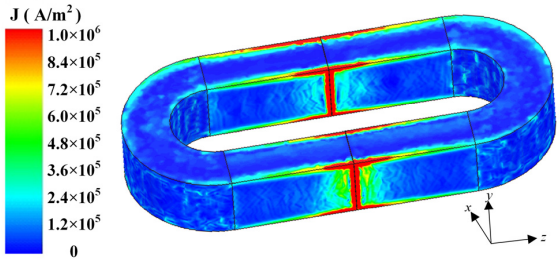


Fig. 5. Distribution of eddy current density at $t = 13.5$ ms.

As shown in Fig. 4, when the impulse excitation current reaches 5 kA at $t = 6.9$ ms, the average magnetic flux density of the core is 1.89 T. The local highest flux density can reach 1.98 T on the air gap. As a result, the core has reached the extremely saturated state. After the thyristor turning off at $t = 12.4$ ms, eddy current loss of reactor reaches maximum at $t = 13.5$ ms, whose distribution is shown in Fig. 5. The magnetic flux diffracts at the air gap, disperses from the z-axis to the x- and y-axes, and inducts eddy current in the normal planes of the x- and y-axes, resulting in larger eddy current. Because the two yokes of core are in different sides of windings, the magnetic flux and core loss density of the inner core are obviously larger than those of the outer core.

At $t = 13.5$ ms, the changing rate dB/dt reaches the maximum, and the corresponding core loss distribution is shown in Fig. 6, which presents three characteristics.

1) Core loss concentrates on the innermost and the outermost silicon steel sheets in the stacking direction (x-axis) due to skin effect.
2) The leakage flux near the air gap causes the macro eddy current so as to bring extra significant core loss.
3) Moreover, the loss of inner core yoke wounded by windings is obviously greater than that of the outer because of the stronger magnetic field intensity. The calculation results of core loss are shown in Table II.

TABLE II
TOTAL CORE LOSS OF THE ANODIC SATURABLE REACTOR

Core loss [W]	Hysteresis loss [W]	Eddy loss [W]	Excess loss [W]
524.25	91.71	284.49	148.05

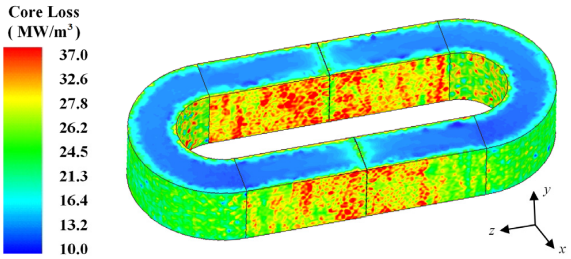


Fig. 6. Distribution of core loss density at $t = 13.5$ ms.

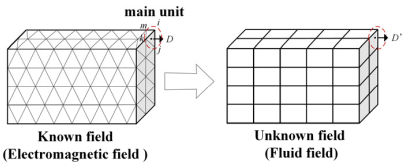


Fig. 7. Data mapping between heterogeneous meshes.

IV. DATA TRANSFER BETWEEN HETEROGENEOUS MESHES

In traditional magneto-thermal coupling method, the heat source is obtained by integrating core loss over one cycle of the whole core region and then distributing it evenly to each element in fluid field. This coupling method with equally distributed loss density underestimates the hottest spot so as not to be accurate enough for the temperature calculation of reactor. Nevertheless, the node-to-node mapping method can allocate loss by actual distribution and predict the temperature distribution inside the saturable reactor more precisely.

As shown in Fig. 7, the element in electromagnetic field is tetrahedron, while the element in the solid region of fluid field is hexahedron. Namely, the meshes of the two physical fields are heterogeneous, so the data cannot be shared directly. To address this, the interpolation method is adopted between the adjacent nodes which belong to the same element in geometry but different physics fields in numeral calculation.

Many methods have been developed to solve this problem, such as nearest neighbor interpolation [10], fast-mapping [11], and radial basis mapping [12]. The principle of the nearest neighbor method is simple, but with lower accuracy especially to sparse mesh. Radial basis function (RBF) method has clear mathematical concept and high calculation accuracy. However, RBF has low precision on the node with small value when the fluctuation range of values is large.

Based on the theory of isoparametric element, the fast-mapping algorithm is a local form of interpolation method. For each node D′ in unknown field, the corresponding node D of known field can be found. The element containing D is called main unit. Then the physical quantity of node D can be obtained by the interpolation of the corresponding physical quantity of each node in the main unit.

Authorized licensed use limited to: Hebei University of Technology. Downloaded on February 20,2022 at 13:09:28 UTC from IEEE Xplore. Restrictions apply.

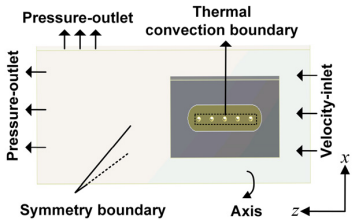
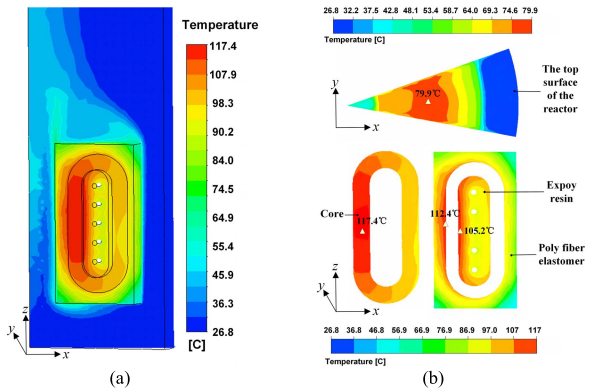


Fig. 8. Boundary conditions setting.



(a) (b)

Fig. 9. Temperature distributions of saturable reactor. (a) Global temperature distribution. (b) Local temperature distribution.

For electromagnetic field, the main unit for node D is tetrahedral element which is consisted of nodes i, j, k, m in Fig. 7. When the linear interpolation is adopted, the heat source density P_{D} of node D can be expressed as follows:

$$P_{\mathrm{D}}(x, y, z) = \sum_{i=1}^{4} N_i^{\mathrm{e}} P_i \tag{15}$$

where P_i denotes the core loss of node i ($i = 1, 2, 3, 4$), N_i^{e} is the shape function of tetrahedron element as follows:

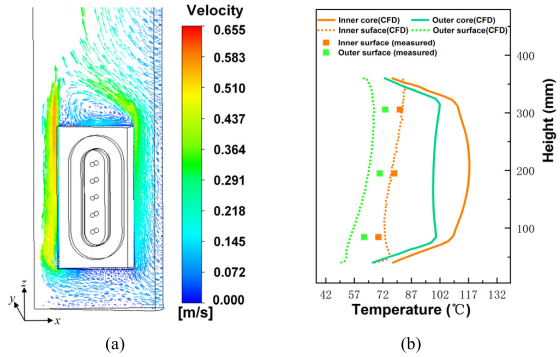
$$N_i^{\mathrm{e}} = \frac{1}{6V}(a_i + b_i x + c_i y + d_i z). \tag{16}$$

V is the volume of tetrahedral element. a_i, b_i, c_i, d_i are the coordinate coefficients of node i. When $i = 1$, a_1, b_1, c_1, d_1 can be calculated by the following equation. For the other a_i, b_i, c_i, d_i can be obtained by replacing the following four determinants in the order of 1, 2, 3, 4 in turn:

$$a_1 = -\begin{vmatrix} x_2 & x_3 & x_4 \\ y_2 & y_3 & y_4 \\ z_2 & z_3 & z_4 \end{vmatrix} \quad b_1 = -\begin{vmatrix} 1 & 1 & 1 \\ y_2 & y_3 & y_4 \\ z_2 & z_3 & z_4 \end{vmatrix}$$
$$c_1 = -\begin{vmatrix} 1 & 1 & 1 \\ x_2 & x_3 & x_4 \\ z_2 & z_3 & z_4 \end{vmatrix} \quad d_1 = -\begin{vmatrix} 1 & 1 & 1 \\ x_2 & x_3 & x_4 \\ y_2 & y_3 & y_4 \end{vmatrix}. \tag{17}$$

V. Calculation of Temperature Field and Fluid Filed

The outside surfaces of the reactor dissipate heat by natural convection, while the inside surfaces of the reactor can transfer the heat by forced cooling water flooded through the hollow aluminum tubes. Because of the geometric symmetry of the reactor, a one-ninth model of saturable reactor shown in Fig. 1(b) is established for temperature simulation. According to Boussinesq hypothesis, the equations about natural convection can be expressed as follows:



(a) (b)

Fig. 10. Temperature field simulation and measured results. (a) Velocity distribution. (b) Temperature curves of CFD and experiment.

$$\rho\left(\frac{\partial \boldsymbol{u}}{\partial t} + \boldsymbol{u}\nabla \cdot \boldsymbol{u}\right) = -\nabla p + \nabla \cdot \boldsymbol{\tau} - \rho \boldsymbol{g} + \boldsymbol{F} \tag{18}$$
$$(\rho - \rho 0)\boldsymbol{g} = \rho 0 \beta (T - T0)\boldsymbol{g} \tag{19}$$

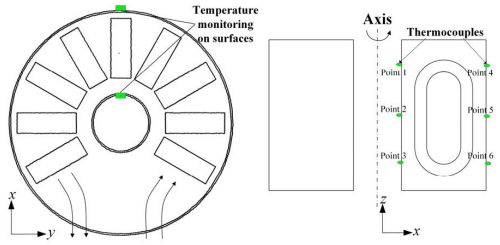
where $\boldsymbol{u}$ represents the velocity of air, ρ is the air density, p is static pressure, $\boldsymbol{\tau}$ is stress tensor, $\boldsymbol{F}$ is body force. In the body force terms, the fluid density is linear as (19), where ρ_0 is air density, and β is body expansion coefficient.

The heat sources of saturable reactor are consisted of core loss and hollow aluminum windings loss. Since the temperature in aluminum windings is lower than that in epoxy resin and core, and the cooling water inside windings is a fluid with stable flow velocity, the windings can be regarded as an internal thermal convection transfer boundary condition and the thermal convection transfer coefficient can be considered as a constant. By the experiment of [13], the thermal convection transfer coefficient on the windings interface increases gradually and stabilizes around 6 W/(m^2·K) finally. The experiment is measured under the condition of 30 °C air and 40 °C cooling water. Contacting with air, the exterior surfaces of reactor dissipate heat by natural convection. Other boundary conditions of the one-ninth model are shown in Fig. 8. The thermal conductivities of core, epoxy resin, polyurethane elastomer and fiberglass are 28, 0.276, 0.55, and 0.23 W/(m·K), respectively.

The temperature distribution of the saturable reactor is shown in Fig. 9. Because of the concentrated local loss and narrow cooling airway, the core situated inside the windings shows higher temperature than that situated outside. The air heated by the warm surface flows upward for the buoyancy resulting from density difference. In z-direction, the thermal convection transfer capacity between the air and the wall decreases gradually. As a result, the hottest spot of core is at the upper middle of inner yoke with 117.4 °C. The temperature of the reactor inner toroidal surface next to the core is 80.5 °C.

As shown in Fig. 10(a), the inner air is heated significantly by inner surface and flows fast in limited space. Meanwhile, the external air gradually rises with the heating effect. When reaching to the top, the air flow is no longer hindered by the solid wall so as to form a backflow. Then the two streams of fluid converge and continue to flow upward for lower pressure

Authorized licensed use limited to: Hebei University of Technology. Downloaded on February 20,2022 at 13:09:28 UTC from IEEE Xplore. Restrictions apply.



(a) (b)

Fig. 11. Temperature measuring experiment. (a) Temperatures of inner and outer toroidal surfaces near the middle core are tested. (b) Schematic of thermocouples laying positions.

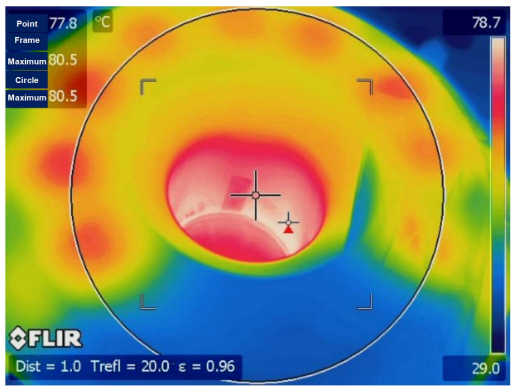


Fig. 12. Temperature measuring experiment by the infrared thermal imager.

TABLE III
TEMPERATURE MEASURED RESULTS ON THERMOCOUPLES

Point 1	Point 2	Point 3	Point 4	Point 5	Point 6
80.8 [°C]	77.8 [°C]	69.5 [°C]	73.1 [°C]	70.2 [°C]	62.3 [°C]

and form a thermal convection cycle with the surrounding air. Fig. 10(b) are temperature curves by CFD simulation of inner core, inner surface, outer core, and outer surface and experiment measurement results of inner and outer surface. The temperature at the inner saturable reactor is higher than the outside no matter the core or shell surface. The inner core temperature distribution curve is protuberated in the middle, since it is the point having concentrated eddy current loss. The experimental results show the effectiveness of the simulation.

VI. EXPERIMENTAL RESULTS

To detect the temperature change of the saturable reactor, the middle core is selected as the test object shown in Fig. 11(a). Three thermocouples are laid on the inner toroidal surface of the shell at the position of 50, 160, and 270 mm, respectively, while the other three thermocouples are laid on the outer surface at the same height shown in Fig. 11(b). Additionally, the infrared thermal imager is used to measure the global temperature of the reactor surface. The temperature measured results are shown in Table III.

With the opening of the thyristor, the impulse excitation current is injected into the reactor windings. When the overall temperature is stable, the infrared thermal imager is used to record the temperature distribution on the reactor shell. Fig. 12 shows that the highest temperature on the shell is in the inner toroidal surface, which is 80.5 °C and in good agreement with CFD simulation results.

VII. CONCLUSION

1) By dynamic loss calculation model, the core loss is mainly distributed on the core surfaces caused by the skin effect and the lamination structure of the core. The core loss density is higher at the position near the air gap for the macro eddy loss induced by leakage flux. The inner core yoke closer to the windings has a higher loss density than the outer one.
2) The distributions of temperature and velocity are obtained by CFD. The hottest spot is located at the air gap of inner core arm with 117.4 °C. The hottest temperature on the reactor inner toroidal surface is 80.5 °C. The core loss calculation method is validated by the temperature measuring experiment.

ACKNOWLEDGMENT

This work was supported in part by the National Natural Science Foundation of China under Grant 51807048 and Grant 51690181, in part by Hebei Province Science Foundation under Grant E2018202284 and Grant E2018202301, and in part by the Creative Research Groups of Hebei Province under Grant E2020202142.

REFERENCES

[1] P. Chen, B. Sun, and F. Ji, "Fault mode analysis and accelerated life test method of the saturable reactor prototype for ±1100 kV UHVDC converter valves," *High Voltage Eng.*, vol. 42, no. 8, pp. 2612–2617, 2016.
[2] Z. Yang *et al.*, "Stress analysis and reliability calculation of saturable reactor of HVDC converter valve in HEMP environment," in *Proc. IEEE 10th Int. Symp. Power Electron. Distrib. Gener. Syst. (PEDG)*, Xi'an, China, Jun. 2019, pp. 294–298.
[3] J. Cao, F. Ji, J. Liu, and P. Chen, "Valve saturable reactor iron losses of ultrahigh-voltage direct current converter," *IET Sci., Meas. Technol.*, vol. 10, no. 2, pp. 77–83, Mar. 2016.
[4] W. Gong, S. Huang, and Y. Yang, "Realization of the method of extracting iron loss coefficient of silicon steel sheet in ANSYS Maxwell," *Motor Control Appl.*, vol. 43, no. 4, pp. 82–85, 2016.
[5] G. Novak, J. Kokosar, A. Nagode, and D. S. Petrovic, "Core-loss prediction for non-oriented electrical steels based on the Steinmetz equation using fixed coefficients with a wide frequency range of validity," *IEEE Trans. Magn.*, vol. 51, no. 4, pp. 1–7, Apr. 2015.
[6] D. Lin, P. Zhou, Q. M. Chen, N. Lambert, and Z. J. Cendes, "The effects of steel lamination core losses on 3D transient magnetic fields," *IEEE Trans. Magn.*, vol. 46, no. 8, pp. 3539–3542, Aug. 2010.
[7] P. Zhou, D. Lin, C. Lu, N. Chen, and M. Rosu, "A new algorithm to consider the effects of core losses on 3-D transient magnetic fields," *IEEE Trans. Magn.*, vol. 50, no. 2, pp. 365–368, Feb. 2014.
[8] S. Barg, K. Ammous, H. Mejbri, and A. Ammous, "An improved empirical formulation for magnetic core losses estimation under nonsinusoidal induction," *IEEE Trans. Power Electron.*, vol. 32, no. 3, pp. 2146–2154, Mar. 2017.
[9] D. Lin, P. Zhou, W. N. Fu, Z. Badics, and Z. J. Cendes, "A dynamic core loss model for soft ferromagnetic and power ferrite materials in transient finite element analysis," *IEEE Trans. Magn.*, vol. 40, no. 2, pp. 1318–1321, Mar. 2004.
[10] P. Thévenaz, T. Blu, and M. Unser, "Interpolation revisited," *IEEE Trans. Med. Imag.*, vol. 17, no. 7, pp. 739–758, Jul. 2000.
[11] W. Dettmer and D. Perić, "A computational framework for fluid-structure interaction: Finite element formulation and applications," *Comput. Methods Appl. Mech. Eng.*, vol. 195, pp. 5754–5799, Aug. 2006.
[12] M. D. Buhmann, *Radial Basis Functions: Theory and Implementations*. Cambridge, U.K.: Cambridge Univ. Press, 2003.
[13] Y. Mi, S. Deng, and L. Gui, "Simulation study on iron-core loss and temperature distribution of saturable reactor for ±1100 kV UHVDC converter valves," *High Voltage Eng.*, vol. 44, no. 10, pp. 3359–3367, 2018.

Authorized licensed use limited to: Hebei University of Technology. Downloaded on February 20,2022 at 13:09:28 UTC from IEEE Xplore. Restrictions apply.